Computational Approaches to Understanding Surface Heat Flow, the Metamorphic Rock Record, and Subduction Geodynamics

by

Buchanan C. Kerswell

A dissertation

submitted in partial fulfillment

of the requirements for the degree of

Doctor of Philosophy in Geosciences

Boise State University

November 2021

BOISE STATE UNIVERSITY GRADUATE COLLEGE

DEFENSE COMMITTEE AND FINAL READING APPROVALS

of the dissertation submitted by

Buchanan C. Kerswell

Dissertation Title: Computational Approaches to Understanding Surface Heat Flow, the Metamorphic Rock Record, and Subduction Geodynamics

Date of Final Oral Examination: August 27, 2021

The following individuals read and discussed the dissertation submitted by student Buchanan C. Kerswell, and they evaluated the student's presentation and response to questions during the final oral examination. They found that the student passed the final oral examination.

Matthew J. Kohn Ph.D.	Chair, Supervisory Committee
C.J. Northrup Ph.D.	Member, Supervisory Committee
H.P. Marshall Ph.D.	Member, Supervisory Committee
Philippe Agard Ph.D.	External Member, Supervisory Committee

The final reading approval of the dissertation was granted by Matthew J. Kohn Ph.D., Chair of the Supervisory Committee. The dissertation was approved by the Graduate College.

DEDICATION

To my mentors, colleagues, friends, and loved ones who take special interests in my life.

This work is yours as much as it is mine.

ACKNOWLEDGMENT

This work was only possible through the efforts of many individuals. My advisor, Dr. Matthew Kohn, deserves special recognition for his contributions, mentorship, and relentless support during the course of my studies. Dr. Taras Gerya and the Geophysical Fluid Dynamics group at the Institut für Geophysik, ETH Zürich, generously offered their high-performance computing resources from the Euler cluster, invaluable instruction, discussion, and support on the numerical modelling methods, and many free meals in Zürich. Additional high-performance computing support from the Borah cluster was provided by the Research Computing Department at Boise State University. Thanks to Dr. D. Hasterok for providing references and guidance on citing the large dataset in chapter three. Special thanks to Dr. Philippe Agard, Dr. Laetitia Le Pourhiet, and graduate students at Sorbonne Université for their incredible expertise and showing me the best of summertime Paris. Thanks to many anonymous reviewers, graduate students, and colleagues for helpful comments on technical aspects of each chapter. My deep appreciation of metamorphic rocks and Alpine geology was formed thanks to outstanding field excursions expertly guided by EFIRE and ZiP graduate students, faculty, and affiliates. Funding for this work was provided by the National Science Foundation grant OIA1545903 awarded to Dr. Matthew Kohn, Dr. Sarah

Penniston-Dorland, and Dr. Maureen Feineman. Datasets and code for reproducing this research are available at https://github.com/buchanankerswell.

ABSTRACT

Pressure-temperature-time (PTt) estimates from high-pressure (HP) metamorphic rocks and global surface heat flow (SHF) rates evidently encode information about pressure-temperature-strain (PTS) fields deep in subduction zones (SZs). Previous work demonstrates the possibility of decoding such geodynamic information by comparing physics-based numerical models with empirical observations of SHF and the metamorphic rock record. However, antithetical interpretations of (non)uniformity with respect to PTS fields are emerging from this line of inquiry. For example, while mechanical coupling depths (CDs) inverted from SHF are narrowly distributed among SZs, maximum pressure-temperature (PT) conditions inverted from exhumed metamorphic rocks are relatively wide-ranging, and yet also uniformly distributed across pressures up to 2.4 GPa. This dissertation scrutinizes (dis)similarities among SZs inferred from large numerical and empirical datasets by applying a variety of computational techniques. First, CDs for 13 modern SZs are predicted after observing coupling in 64 numerical geodynamic simulations. Second, spatial patterns of SHF are assessed in two-dimensions by interpolating thousands of SHF observations near several SZ segments. Third, PTt distributions of over one million markers traced from the previous set of 64 SZ simulations are compared with hundreds of empirical PTt estimates from the rock record to assess the effects of thermo-kinematic boundary conditions (TKBCs) on deep mechanical processing of rock in SZs. These studies conclude the following. Mechanical coupling between plates is primarily controlled by the upper plate lithospheric thickness, with marginal responses to other TKBCs. SHF interpolations show high variance within and among SZ segments, suggesting local, rather than widespread, continuity of PTS fields deep within SZs. Computed marker recovery rates correlate with TKBCs, and are therefore expected to vary among SZs. Finally, computed PTt distributions of markers show patterns consistent with transient, localized recovery from a cooling, serpentinizing plate interface. Together, this work encourages more antireductionist and diversified views of subduction geodynamics until SHF and PTt datasets can more precisely distinguish (dis)similarities in PTS fields within and among SZs. Strategically scaling PTt and SHF datasets in the future will improve computational precision and confidence, and thus will advance subduction zone research.

TABLE OF CONTENTS

LIST OF FIGURES

LIST OF TABLES

LIST OF ABBREVIATIONS

CD coupling depth

HP high-pressure

PT pressure-temperature

PTS pressure-temperature-strain

PTt pressure-temperature-time

SHF surface heat flow

SZ subduction zone

TKBCs thermo-kinematic boundary conditions

UPT upper plate thickness

LIST OF SYMBOLS

GPa Gigapascal

K Kelvin

Ma *Mega annum* or million-years

Z_{UP} Upper plate thickness

Z_{cpl} Mechanical coupling depth

Φ Thermal parameter

η viscosity

$\vec{q}$ surface heat flow

$\vec{v}_{conv}$ convergence velocity

$^{\circ}C$ Celcius

km kilometer

t_{OP} oceanic plate age

$wt.\%$ weight percent

CHAPTER 1:

INTRODUCTION

Keypoints:

- Proxy datasets are key for inference about geodynamics deep in SZs
- Computation leverages large data to infer, build, and test geodynamic models

CHAPTER 2:

EFFECTS OF THERMO-KINETIC BOUNDARY CONDITIONS ON MECHANICAL PLATE COUPLING IN SUBDUCTION ZONES

Keypoints:

- Mechanical coupling responds strongly to upper plate thickness (UPT)
- Inverting surface heat flow (SHF) allows coupling depth (CD) estimation
- Globally consistent SHF implies consistent UPT, and thus uniform CDs

2.1 Abstract

Deep mechanical coupling between converging plates is implicated in plate motions, crustal deformation, seismic cycles, arc magmatism, detachment of subducting material, and is considered a key feature of subduction zone (SZ) geodynamics. This study uses two-

dimensional numerical models of oceanic-continental convergent margins to investigate effects of thermo-kinematic boundary conditions (TKBCs) on coupling—specifically focusing on thermal parameter (Φ) and upper plate thickness (UPT). Numerical experiments implement coupling by including the metamorphic (de)hydration reaction $antigorite \Leftrightarrow olivine + orthopyroxene + H_2O$ in the upper-plate mantle. Visualizing pressure-temperature-strain (PTS) fields show thermal feedbacks regulating coupling depth (CD) dynamically with strong responses to UPT and weak responses to Φ. The results imply estimation of CD is possible by inverting UPT from surface heat flow (SHF). Moreover, SHF sampled from the backarc region near 13 modern SZs imply consistent UPT, and thus uniform CDs among SZs.

2.2 Introduction

Subduction geodynamics are largely defined by plate motions and mechanical behaviour along the plate interface. For example, a transition from mechanically decoupled (moving differentially with respect to each other) to coupled plates (moving with the same local velocity) dramatically increases temperature by inducing mantle circulation in the upper plate (Peacock *et al.*, 1994; Peacock, 1996). Observations from numerical experiments and forearc SHF imply coupling transitions occurring globally within a narrow range of depths in modern SZs (70-80 *km*). Further, coupling appears essentially unresponsive to important TKBCs, including oceanic-plate age, convergence velocity, and subduction geometry (Furukawa, 1993; Wada *et al.*, 2008; Wada & Wang, 2009). While uniform CDs among SZs are inferred from different datasets, this phenomenon remains curious and unconfirmed to a large extent. To understand SZ geodynamics, it is essential to understand why modern subduction zones appear to achieve similar CDs despite differences in their physical characteristics.

Notwithstanding, many numerical geodynamic models use CDs of 70-80 *km* as a boundary condition (Abers *et al.*, 2017; Currie *et al.*, 2004; Syracuse *et al.*, 2010; van Keken *et al.*, 2011, 2018; Wada *et al.*, 2012; Gao & Wang, 2014; Wilson *et al.*, 2014), although not exclusively (e.g. 40-56 *km*, England & Katz, 2010; Peacock, 1996). Similar CDs among SZs is an attractive hypothesis for at least two reasons. First, it helps explain a relatively narrow range of depths to subducting oceanic-plates beneath volcanic arcs (England *et al.*, 2004; Syracuse & Abers, 2006) as mechanical coupling is expected to be closely associated with the onset of flux melting. Second, mechanical coupling is required to detach crustal fragments from the subducting plate (Agard *et al.*, 2016), so uniform CDs may also help explain why maximum pressures recorded by subducted oceanic material worldwide is $\leq$ 2.3-2.5 *GPa* (roughly 80 *km*, Agard *et al.*, 2009, 2018).

The location and extent of mechanical coupling along the plate interface is implicated in myriad geodynamic phenomena, including seismicity, metamorphism, volatile flux, volcanism, plate motions, and crustal deformation (Čížková & Bina, 2013; Gonzalez *et al.*, 2016; Hirauchi *et al.*, 2010; Peacock, 1990, 1991, 1993, 1996; Peacock & Hyndman, 1999; Hacker *et al.*, 2003; van Keken *et al.*, 2011; Grove *et al.*, 2012; Gao & Wang, 2017).

Consequently, the mechanics of coupling have been extensively studied and discussed. Coupling fundamentally depends on the strength (viscosity) of materials above, within, and below the plate interface. Water flux from compaction and dehydration of hydrous minerals with increasing pressure-temperature (PT) forms layers of low viscosity sheet silicates near the plate interface. Transmission of shear stress between plates is inhibited by formation of talc and serpentine in the shallow upper-plate mantle (Peacock & Hyndman, 1999). Lack of traction along the interface, combined with cooling from the subducting plate surface, ensures a positive feedback between hydrous mineral formation and mechanical decoupling. Experimentally determined flow laws, petrologic observations, and geophysical observations all support the plausibility of this conceptual model of subduction interface behaviour (e.g., Agard *et al.*, 2016, 2018; Gao & Wang, 2014; Peacock & Hyndman, 1999).

Experimental control over important TKBCs makes numerical modelling essential for investigating such complex geodynamic environments. Wada & Wang (2009) previously investigated the effects of Φ on CDs by numerically simulating 17 active subduction zones. Among other TKBCs, their models specify convergence rate, subduction geometry, thermal structure of oceanic- and overriding-plates, and degree of coupling along the subduction interface. Notably, their experiments control for interface rheology and discriminate best-fit CDs based on observed forearc SHF.

This study similarly specifies TKBCs to numerically simulate the range of modern SZ systems, but regulates interface rheology dynamically by implementing metamorphic reactions that respond to evolving PTS fields. Subduction geometry and CD are not fully determined features, in other words, but rather spontaneous model outcomes within the range of specified boundary conditions discussed in section 2.3. As in previous studies (e.g., Ruh *et al.*, 2015), rheological effects of the dehydration reaction $antigorite \Leftrightarrow olivine + orthopyroxene + H_2O$ are implemented to drive mechanical coupling. An abrupt viscosity increase accompanies antigorite destabilization, thereby inducing mechanical coupling, as defined by empirically-determined flow laws used in the experiments (Table 2.1).

This chapter focuses on two fundamental questions. How does CD respond to Φ *and* UPT? And how stable is CD through time? First, 64 convergent margins with variable UPT and Φ are numerically simulated and mechanical plate coupling is observed. Thermal feedbacks within the system are visualized in terms of mantle temperature, viscosity, and velocity fields and CD responses to a range of Φ and UPT are quantified using multi-variate linear regression. Three different regression models are then used to predict CDs for 13 modern SZs, which all predict similarly narrow ranges of CDs. Implications and questions about UPT and CD uniformity among SZs are finally discussed before further investigation into SHF in Chapter 3.

2.3 Numerical modelling methods

This study simulates converging oceanic-continental plates, where an ocean basin is being consumed by subduction at a continental margin (Figure 2.1). Initial conditions are modified from previous numerical experiments of active margins (Sizova *et al.*, 2010; Gorczyk *et al.*,

2007) using the code `I2VIS` (Gerya & Yuen, 2003), although plate coupling was not the focus of their studies. Identical rheologic model, material properties (Table2.1), and hydration/melt model (Table A.1 & Appendix A.1) as Sizova *et al.* (2010) are used. However, the version of `I2VIS` in this study differs from Sizova *et al.* (2010) in its initial setup, overall dimension, resolution, continental geotherm, dehydration model, and left boundary condition (origin of new oceanic lithosphere). Differences are outlined in this section and in Appendix A.1. Sixty-four `I2VIS` models constructed with varying convergence rates ($\vec{v}_{conv}$), oceanic-plate ages (t_{OP}), and UPTs (Figure 2.2) were ran on the Euler cluster at ETH, Zürich until achieving at least 10 Ma of subduction.

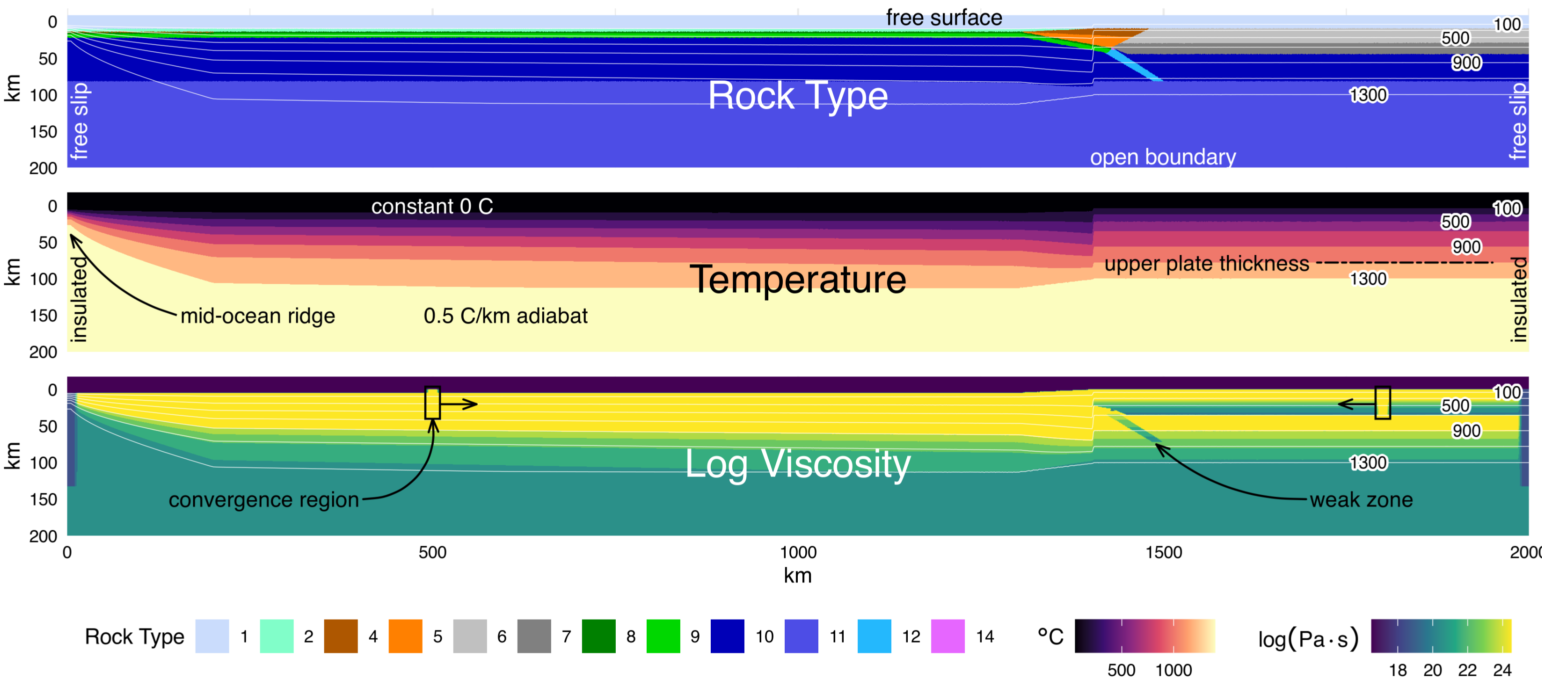

Figure 2.1: Initial model configuration and boundary conditions. (a) A free sedimentation/erosion boundary at the surface is maintained by implementing a layer of "sticky" air and water, and an infinite-like open boundary at the bottom allows for spontaneous oceanic-plate descent and subduction angle. Left and right boundaries are free slip and thermally insulating. Initial material distribution includes 7 *km* of oceanic crust (2 *km* basalt, 5 *km* gabbro), 1 *km* of oceanic sediments, and 35 *km* of continental crust, thinning ocean-ward. (b) Oceanic lithosphere is continually created at the left boundary. The oceanic geotherm is calculated using a half-space cooling model and the continental geotherm is calculated using a one-dimensional steady-state conductive cooling model to 1300 $^{\circ}C$. The base of the upper plate lithosphere (Z_{UP}) is defined by visualizing viscosity and generally coincides with the 1100 $^{\circ}C$ isotherm. (c) Oceanic crust is bent under loading from passive margin sediments, and a weak zone extends through the lithosphere to help induce subduction. Convergence velocities are imposed at stationary, high-viscosity regions far from the trench. Rock type colors are: [1] air, [2] water, [4,5] sediments, [6,7] felsic crust, [8] basalt, [9] gabbro, [10,11] dry mantle, [12] hydrated mantle, [14] serpentinized mantle.

2.3.1 Initial setup and boundary conditions

Simulations are 2000 *km* wide and 300 *km* deep (Figure 2.1). In the model domain, three governing equations of heat transport, momentum, and continuity are discretized and solved with a conservative finite-difference marker-in-cell approach on a fully staggered grid as outlined in Gerya & Yuen (2003). Numerical resolution is non-uniform with higher resolution (1 *km* x 1 *km*) in a 600 *km* wide area surrounding the contact between the oceanic-plate and continental margin, then gradually changing to lower resolution towards the model boundaries (5 *km* x 1 *km*, x- and z-directions, respectively). The left and right boundaries are free-slip and thermally insulating (Figure 2.1a, b). Implementation of "sticky" air and water allows for a free topographical surface with a simple linear sedimentation and erosion model. The lower boundary is open to allow for oceanic-plate descent with a spontaneous subduction angle (Burg & Gerya, 2005).

A horizontal convergence force is applied to both plates in a rectangular region far from the continental margin (Figure 2.1c). An initial weak layer cutting the lithosphere permits subduction to initiate. The high-viscosity ($\eta = 10^{25}\ Pa \cdot s$) rectangular convergence regions apply constant horizontal velocities without deforming the lithosphere. Subduction angle is governed by free-motion of the subducting plate. Similarly, subduction velocity varies with time in response to extension or shortening of the overriding plate. Φ is thus calculated as the product of the horizontal convergence velocity and the oceanic-plate age (c.f. McKenzie, 1969). For convenience and consistency with the literature, this study presents Φ in units of *km*/100 (Figure 2.2a).

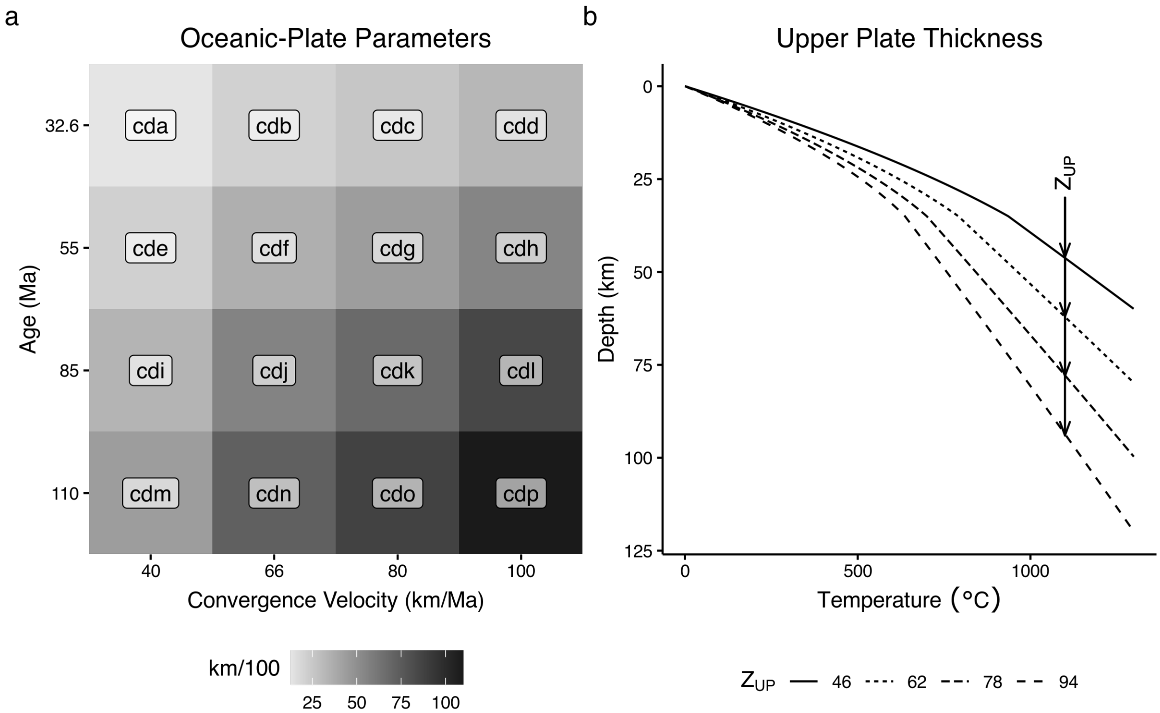

Figure 2.2: Range of thermo-kinematic boundary conditions used in numerical experiments. (a) Thermal parameters (grayscale) range from 13 to 110 $km/100$ and broadly reflect the distribution of oceanic-plate ages and convergence velocities in modern subduction zones. Model names include the prefix "cd" for "coupling depth" with increasing alphabetic suffixes. Note that neither axes are continuous. (b) Upper plate thickness (Z_{UP}) is defined by a range of continental geotherms. Geotherms were constructed using a one-dimensional steady-state conductive cooling model with $T(z=0)$ = 0 $^{\circ}C$, $\vec{q}(z=0)$ = 59, 63, 69, 79 mW/m^2, and constant radiogenic heating of 1.0 $\mu W/m^3$ for a 35 km-thick crust and 0.022 $\mu W/m^3$ for the mantle. Continental geotherms are calculated up to 1300 $^{\circ}$C with a constant 0.5 $^{\circ}C/km$ gradient (the mantle adiabat) extending to the base of the model domain.

2.3.2 Calculating geotherms and defining lithospheric thickness

Oceanic crust is modeled as 1 *km* of sediment cover overlying 2 *km* of basalt and 5 *km* of gabbro (Figure 2.1a). Oceanic lithosphere is continually made at a pseudo-mid-ocean ridge at the left boundary of the model (Figure 2.1b). An enhanced vertical cooling condition applied at 200 *km* from left boundary adjusts for the proper oceanic-plate age, and therefore its lithospheric thickness as it enters the trench (Agrusta *et al.*, 2013). Oceanic-plate ages range from 32.6 to 110 Ma and convergence velocities from 40 to 100 km/Ma (Figure 2.2a). This range of parameters broadly reflects the middle-range of modern global subduction systems (Syracuse & Abers, 2006).

Initial continental geotherms are determined by solving the heat flow equation in one-dimension to 1300 $°C$ (Figure 2.2b). This study assumes a fixed temperature of 0 $°C$ at the surface, constant radiogenic heating of 1 $\mu W/m^3$ in the 35 km-thick continental crust, 0.022 $\mu W/m^3$ in the mantle, with thermal conductivities of 2.3 W/mK and 3.0 W/mK for the continental crust and mantle, respectively. Above, 1300 $°C$, temperature is assumed to constantly increase by 0.5 $°C/km$ (the mantle adiabat) to the base of the model domain.

Many studies define the base of the continental lithosphere at the 1300 $°C$ isotherm, but it can be determined directly by visualizing viscosity and strain rate as the model progresses. The mechanical base of the lithosphere (Z_{UP}) in the models generally occurs near the 1100 $°C$ isotherm—characterized by a rapid decrease in viscosity and increase in strain rate (Figures **??**, **??**, **??**). As such, this study considers oceanic and continental lithospheres as mechanical layers defined by viscosity, rather than defined merely by temperature. Z_{UP} corresponding to backarc surface heat flow of 59, 63, 69, and 79 mW/m^2 are used in this study (Figure 2.2b).

2.3.3 Metamorphic (de)hydration reactions

Using Lagrangian markers (Harlow, 1962, 1964) to store and update material properties and PTS fields allows for straight-forward numerical implementation of metamorphic reactions. This approach is key to regulating mechanical coupling dynamically in SZ simulations. For example, dehydration (eclogitization) of the oceanic-plate and (de)stabilization of antigorite in the upper-plate mantle may be effectively modelled by tracing marker PTt paths while changing marker properties according to thermodynamically-stable mineral assemblages (e.g., Connolly, 2005). For computational efficiency, however, water contents in this study are not computed by iteratively solving thermodynamic systems of equations. Instead, gradual eclogitization of oceanic crust is computed as a linear function of lithostatic pressure to a maximum depth of 150 km, or temperature of 1427 $^{\circ}C$, while including garnet-in and plagioclase-out reactions defined by Ito & Kennedy (1971). Mantle (de)hydration is computed according reactions boundaries defined by Schmidt & Poli (1998) with a maximum water content of 2 $wt.\%$ (explained below). This approach effectively simulates continuous influx of water to the upper-plate mantle with relatively low computational cost, beginning with compaction and release of connate water at shallow depths, followed by a sequence of reactions consuming major hydrous phases (chlorite, lawsonite, zoisite, chloritoid, talc, amphibole, and phengite) in different parts of the hydrated basaltic crust (Schmidt & Poli, 1998; van Keken *et al.*, 2011).

The extent of metamorphic reaction effects on mechanical coupling, and the exact (de)hydration reaction(s) likely responsible, are unknown. However, formation of brucite and serpentine from dry olivine near the plate interface are inferred to strongly regulate mechanical behaviour (Hyndman & Peacock, 2003; Peacock & Hyndman, 1999; Agard *et al.*, 2016). Brucite notably breaks down at much lower temperatures than serpentine (Schmidt & Poli, 1998), so serpentine (de)stabilization arguably represents the key transition from a weak-to-strong upper-plate mantle deep in SZs. This study elects an implement of antigorite (de)hydration for this reason. The reaction is assumed to be abrupt and discontinuous, which is a fine approximation for near-endmember compositions like (Mg-rich) peridotites. The PT conditions of the reaction $antigorite \Leftrightarrow olivine + orthopyroxene + H_2O$ were numerically implemented by the following equation (after Schmidt & Poli, 1998):

$$T_{atg-out}(z) = \begin{cases} 751.50 + 6.008 \times 10^{-3} z - 3.469 \times 10^{-8} z^2, & \text{for } z < 63000m \\ 1013.2 - 6.039 \times 10^{-5} z - 4.289 \times 10{-}9 z^2, & \text{for } z > 63000m \end{cases} \tag{2.1}$$

where z is the depth of a marker from the surface in meters and T is temperature in Kelvins. This reaction boundary is consistent to within 25 $^\circ C$ of more recent experiments by Shen *et al.* (2015). Markers with internal temperature exceeding $T_{atg-out}(z)$ spontaneously form $olivine + orthopyroxene + H_2O$ and release their crystal-bound water. This implementation tacitly assumes thermodynamic equilibrium and is common to many versions of `I2VIS`.

Oceanic-plates of different ages are also tacitly assumed to dehydrate similarly with the above implementation. However, older (colder) oceanic-plates are expected to carry water to greater depths than younger (warmer) plates because of relatively delayed water-releasing reactions (Peacock, 1996). Abrupt water release at the antigorite dehydration reaction boundary defined by Equation (2.1) was tested to model deep water retention in cold oceanic-plates. Mechanical coupling behaviour was indistinguishable from gradual water release models. This implies rates of water release are less important than the depth of antigorite dehydration. Explicitly modelling other major dehydration reactions are thus unlikely to significantly affect mechanical coupling behaviour, yet likely to introduce numerical artifacts at great computational cost. A simplified gradual water release model for all oceanic-plates is therefore preferred.

Water released by rock forms discrete fluid particles that migrate with relative velocities defined by local deviatoric (non-lithostatic) pressure gradients (see Appendix @ref(!!!), Faccenda *et al.*, 2009). Fluid velocities are scaled by a 10 cm/yr vertical percolation velocity to account for purely lithostatic pressure gradients in the mantle (Gorczyk *et al.*, 2007). Fluid particles migrate until encountering rock that can consume additional water by equilibrium hydration or melting reactions, (Equation A.1).

The shallow upper-plate mantle can theoretically store large amounts of water as antigorite may contain up to 13 $wt.\%$ water (Reynard, 2013) and is generally stable at shallow mantle conditions. Thermodynamic models predict 8 $wt.\%$ water in the shallow upper-plate

Table 2.1: Material properties used in numerical experiments

Material	ρ	H_2O	Flow Law	$log_{10}A$	E	V	n	ϕ	σ_{crit}	k_1	k_2	k_3	H
sediments	2600	5.0	wet quartzite	-3.5	154.0	3.0	2.3	0.15	0.03	0.64	807	4e-06	2.000
felsic crust	2700		wet quartzite	-3.5	154.0	3.0	2.3	0.45	0.03	0.64	807	4e-06	1.000
basalt	3000	5.0	plag an75	-3.5	238.0	8.0	3.2	0.45	0.03	1.18	474	4e-06	0.250
gabbro	3000		plag an75	-3.5	238.0	8.0	3.2	0.45	0.03	1.18	474	4e-06	0.250
mantle dry	3300		dry olivine	4.4	540.0	20.0	3.5	0.45	0.30	0.73	1293	4e-06	0.022
mantle hydrated	3300	0.5	wet olivine	3.3	430.0	10.0	3.0	0.45	0.24	0.73	1293	4e-06	0.022
serpentine	3200	2.0	serpentine	3.3	8.9	3.2	3.8	0.15	3.00	0.73	1293	4e-06	0.022

key: ρ: density $[kg/m^3]$, H_2O: water content $[wt.\%]$, A: material constant, E: activation energy $[kJ/mol]$, V: activation volume $[J/MPa \cdot mol]$, n: power law exponent, ϕ: internal friction angle, σ_{crit}: critical stress $[MPa]$, H: heat production $[\mu W/m^3]$

constants: C_p: heat capacity = 1 $[kJ/kg]$, α: expansivity = 2×10^{-5} $[1/K]$, β: compressibility = 0.045 $[1/MPa]$

thermal conductivity: $k\ [W/m \cdot K] = (k_1 + \frac{k_2}{T+77}) \times exp(k_3 \cdot P)$ with P in $[MPa]$ and T in $[K]$

references: Turcotte & Schubert (2002), Ranalli (1995), Hilairet et al. (2007), Karato & Wu (1993)

mantle (Connolly, 2005). However, seismic studies suggest most shallow upper-plate mantles are only partially serpentinized (< 20-40%), equating to water contents of approximately 3-6 $wt.\%$ (Abers *et al.*, 2017; Carlson & Miller, 2003). Many modes of mantle hydration are documented or inferred, including evidence for channelized fluid flow within ophiolites exhumed from SZs (Angiboust *et al.*, 2012, 2014; Zack & John, 2007; Plümper *et al.*, 2017). This study limits mantle wedge hydration to $\leq 2\ wt.\%\ H_2O$ and assumes any excess H_2O exits the system through channelized fluid flow during plastic or brittle deformation (Davies, 1999).

2.3.4 Rheologic model

Contributions from dislocation and diffusion creep are accounted for by computing a composite rheology for ductile rocks, $\eta_{effective}$:

$$\frac{1}{\eta_{effective}} = \frac{1}{\eta_{diff}} + \frac{1}{\eta_{disl}} \tag{2.2}$$

where η_{diff} and η_{disl} are effective viscosities for diffusion and dislocation creep.

For the crust and serpentinized mantle, η_{diff} and η_{disl} are computed as:

$$\begin{aligned} \eta_{diff} &= \frac{1}{2} A\ \sigma_{crit}^{1-n}\ \exp\left[\frac{E+PV}{RT}\right] \\ \eta_{disl} &= \frac{1}{2} A^{1/n}\ \dot{\varepsilon}_{II}^{(1-n)/n}\ \exp\left[\frac{E+PV}{nRT}\right] \end{aligned} \tag{2.3}$$

where R is the gas constant, P is pressure, T is temperature in K, $\dot{\varepsilon}_{II} = \sqrt{\frac{1}{2}\dot{\varepsilon}_{ij}^2}$ is the square root of the second invariant of the strain rate tensor, σ_{crit} is an assumed diffusion-dislocation transition stress, and A, E, V and n are the material constant, activation energy, activation volume, and stress exponent, respectively (Table 2.1, Hilairet *et al.*, 2007; Ranalli, 1995).

For the mantle, η_{diff} and η_{disl} are computed as (Karato & Wu, 1993):

$$\begin{aligned} \eta_{diff} &= \frac{1}{2} A^{-1}\ G\ \left[\frac{h}{b}\right]^{m/n}\ \exp\left[\frac{E+PV}{RT}\right] \\ \eta_{disl} &= \frac{1}{2} A^{-1/n}\ G\ \dot{\varepsilon}_{II}^{(1-n)/n}\ \exp\left[\frac{E+PV}{nRT}\right] \end{aligned} \tag{2.4}$$

where b=5×10^{-10} m is Burgers vector, G=8×10^{10} Pa is shear modulus, h=1×10^{-3} m is the assumed grain size, $m = 2.5$ is the grain size exponent, and the other flow law parameters are given in Table 2.1. Our models limited viscosity for all rocks at $\eta_{min} = 10^{17}$ $Pa\cdot s$ and

$\eta_{max} = 10^{25}\ Pa \cdot s$.

An effective visco-plastic rheology is achieved by limiting $\eta_{effective}$ with a brittle (plastic) yield criterion:

$$\eta_{effective} \leq \frac{C + \phi\ P}{2\ \dot{\varepsilon}_{II}} \tag{2.5}$$

2.3.5 Visualization and determination of coupling depth

The rheologic model and TKBCs described in the previous sections always results in plate motions towards the left boundary (slab-rollback). Relatively high dip angles and extreme subduction velocities in the some high-Φ experiments cause chaotic behaviour by 10 Ma as the upper-plate is stretched thin and mechanical interference occurs between trench sediments and the high-viscosity convergence region 200 km from the left boundary. Numerical solutions are stable for most experiments, however, reaching quasi-steady state by 5 Ma. An additional 5 Ma is allowed to ensure stable geodynamics before observing CD. Surface heat flow, rock type, temperature, viscosity, strain rate, shear heating, and velocity fields are visualized at approximately 10 Ma (e.g., Figure 2.3) for all 64 experiments to assess geodynamics and solution stability (Figure **??**).

After approximately 10 Ma of subduction CD is determined directly from viscosity by finding the approximate area where strength contrasts between serpentinized- and non-serpentinized upper-plate mantle diminishes to $< 10^2\ Pa \cdot s$. The node nearest to this region is assigned as the CD. This study assumes mechanical coupling occurs instantaneously and at a single node. Mechanical coupling in reality must be dispersed across a finite length along the plate interface, however. At the numerical resolution the experiments, coupling-like viscosity contrasts are similar within a small area (approximately 5x5 *km* or 5x5 nodes), giving a qualitative uncertainty CD on the order of 2.5 *km*.

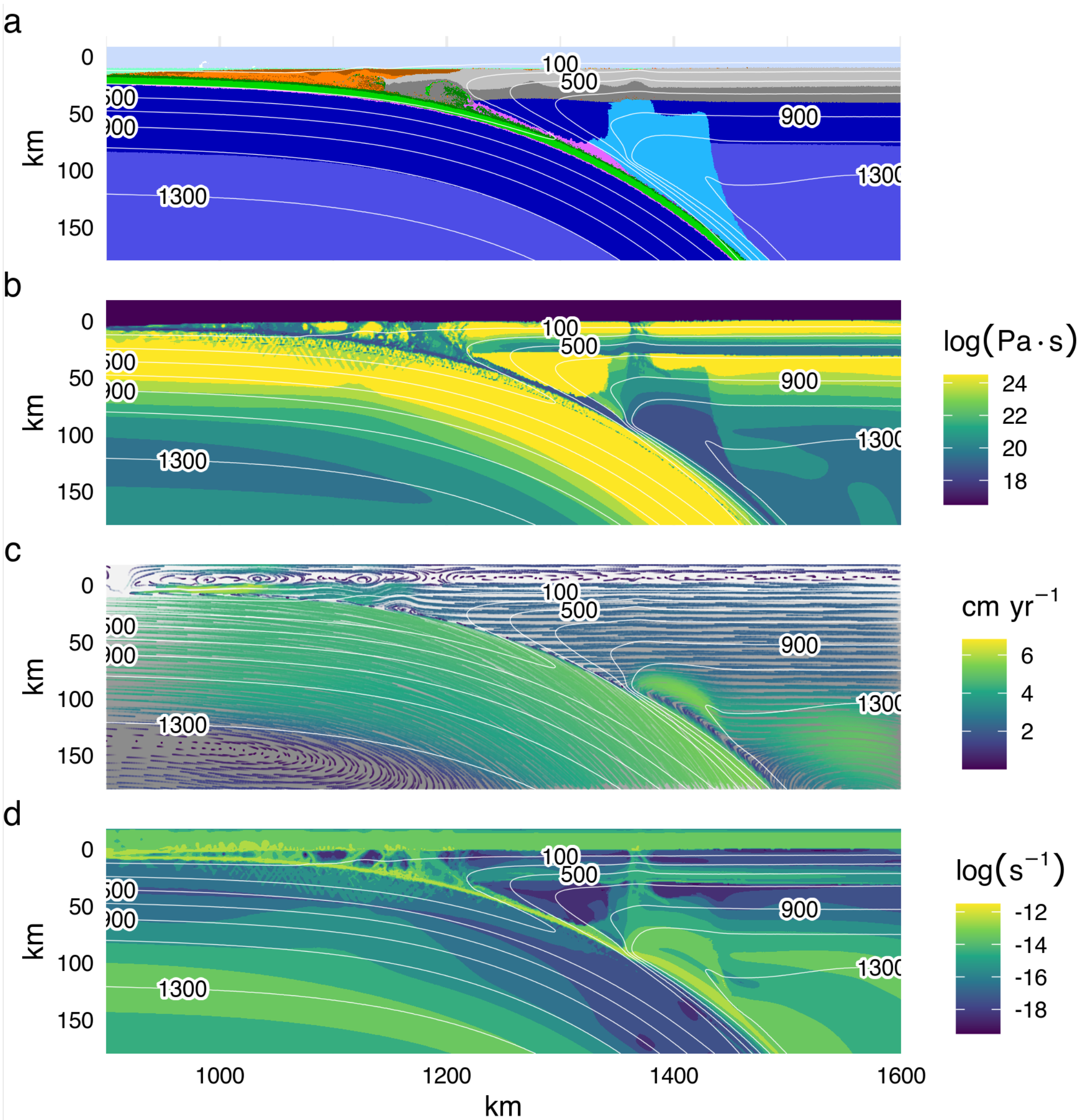

Figure 2.3: Visualization of model cdf with a 78 km upper-plate lithosphere at approximately 10 Ma. (a) Rock type shows a thin serpentine layer (pink) lubricating the plate interface. Note that low melt volumes are inconspicuous and quickly extracted. (b) Viscosity shows high contrast between the oceanic-plate and serpentinized upper-plate mantle at shallow levels. Viscosity contrast disappears where serpentine becomes unstable. (c) Streamlines show focused mantle flow towards the interface, coinciding with the lower limit of serpentine stability. Note the converging isotherms that imply a feedback between heat transfer, serpentine destabilization, and mechanical coupling. (d) Strain rate shows localized deformation in the serpentine layer along the plate interface. Note that deformation in the upper-plate mantle is restricted to viscous flow beneath the lithosphere and along narrow, subvertical melt conduits. Rock type colors are the same as Figure 1.

CHAPTER 3:

A COMPARISON OF HEAT FLOW INTERPOLATIONS NEAR SUBDUCTION ZONES

Keypoints:

- Inconsistent spatial patterns characterize heat flow near subduction zones
- Heat flow investigations favour 2D interpolations over 1D transects
- Scaling datasets and new interpolation schema will advance SZ research

3.1 Abstract

Heat fluxing through the Earth's surface provides indirect observations of pressure-temperature-strain (PTS) fields deep in SZs. Global heat flow databases, therefore, are invaluable for generating and testing belief about SZ geodynamics. Investigating surface heat flow (SHF) in two-dimensions by interpolation, rather than in one-dimension by

projection, arguably forms better interpretations about spatial continuity of deep processes. Direct comparisons of interpolations based on the First (spatial continuity) and Third (similarity) Laws of Geography applied to the most updated global heat flow database. Inconsistent spatial patterns of SHF near SZs are observed in magnitude and variance, regardless of interpolation method. The implications include discontinuous PTS fields at depth, countering hypotheses of commonly thin upper plate lithospheres and mechanical CDs among subduction zones. Strategic scaling of SHF datasets will improve interpolation precision and confidence—leading to better tools for distinguishing differences within and among SZs. New data acquisition and composite interpolation schema are proposed as avenues for future SZ research.

APPENDIX A:

A.1 (De-)hydration model

The material properties used in our experiments are listed in Table 2.1 and Table A.1. For details about the sedimentation and erosion, melting and extraction, and rheological models, please refer to Sizova *et al.* (2010). Here we discuss only the hydrodynamic model, because it is the most relevant aspect of our results.

The hydrodynamics in our models controls the timing and magnitude of mantle wedge hydration. The main sources of water delivered to the mantle are altered basaltic crust and seafloor sediments, which we assumed to contain up to 5 $wt.\%H_2O$. We assumed a gradual expulsion of water from pore space and through quasi-continuous dehydration reactions occurring within the slab. Water content is computed using the following equation:

$$\chi_{H_2O(wt.\%)} = \chi_{H_2O(p_0)} \times \left(1 - \frac{\Delta z}{150 \cdot 10^3}\right) \tag{A.1}$$

where $\chi_{H_2O(p_0)}$=5 $wt.\%$ and Δz is a marker's depth below the topographical surface.

If a rock marker dehydrates, an independent water particle is instantaneously generated at the same location with the respective H_2O content. The new water particle is moved in

Table A.1: Melting curves used in numerical experiments

Material	a	b	c	d	e	f	g	h	i	j
sediments	1200	889	1.79e+04	54	2.02e+04	831	6.00e-02		1262	0.009
felsic crust	1200	889	1.79e+04	54	2.02e+04	831	6.00e-02		1262	0.009
basalt	1600	973	7.04e+05	354	7.78e+07	935	3.50e-03	6.2e-05	1423	0.105
gabbro	1600	973	7.04e+05	354	7.78e+07	935	3.50e-03	6.2e-05	1423	0.105
mantle dry						1394	1.33e-01	-5.1e-05	2073	0.114
mantle hydrated	2400	1240	4.98e+04	323			1.27e+05	3.5e-05	2073	0.114
serpentine	2400	1240	4.98e+04	323			1.27e+05	3.5e-05	2073	0.114

solidus curve: $T(P) = [b + \frac{c}{(P+d)} + \frac{e}{(P+d)^2}]$ at $P < a$ and $[f + gP + hP^2]$ at $P \geq a$
liquidus curve: $T(P) = i + jP$ with T in $[K]$ and P in $[MPa]$
reference: Schmidt & Poli (1998)

accordance to the local velocity field, described by the following equation:

$$
\begin{aligned}
v_{\text{water}} &= \left(v_{x(\text{fluid})}, v_{z(\text{fluid})}\right) \\
v_{z(\text{fluid})} &= v_{z(\text{fluid})} - v_{z(\text{percolation})}
\end{aligned}
\tag{A.2}
$$

where v_{water} is the velocity vector of the water particle, v_x and v_z are the local velocity vectors of the the solid state mantle or crust, and $v_{z(percolation)}$ is a prescribed upward percolation velocity (10 $cm/year$). We implicitly neglect kinetics of reactions, as material properties of markers change instantaneously at equilibrium reactions.

REFERENCES

Abers, G. A., van Keken, P. E., & Hacker, B. R. 2017. The cold and relatively dry nature of mantle forearcs in subduction zones. *Nature Geoscience*, **10**(5), 333–337.

Agard, P., Yamato, P., Jolivet, L., & Burov, E. 2009. Exhumation of oceanic blueschists and eclogites in subduction zones: Timing and mechanisms. *Earth-Science Reviews*, **92**(1-2), 53–79.

Agard, P., Yamato, P., Soret, M., Prigent, C., Guillot, S., Plunder, A., Dubacq, B., Chauvet, A., & Monié, P. 2016. Plate interface rheological switches during subduction infancy: Control on slab penetration and metamorphic sole formation. *Earth and Planetary Science Letters*, **451**, 208–220.

Agard, P., Plunder, A., Angiboust, S., Bonnet, G., & Ruh, J. B. 2018. The subduction plate interface: Rock record and mechanical coupling (from long to short time scales). *Lithos*, **320-321**, 537–566.

Agrusta, R., Arcay, D., Tommasi, A., Davaille, A., Ribe, N., & Gerya, T. 2013. Small-scale convection in a plume-fed low-viscosity layer beneath a moving plate. *Geophysical Journal International*, **194**(2), 591–610.

Angiboust, S, Langdon, R, Agard, P, Waters, D, & Chopin, C. 2012. Eclogitization of the Monviso ophiolite (W. Alps) and implications on subduction dynamics. *Journal of Metamorphic Geology*, **30**(1), 37–61.

Angiboust, Samuel, Pettke, Thomas, De Hoog, Jan CM, Caron, Benoit, & Oncken, Onno. 2014. Channelized fluid flow and eclogite-facies metasomatism along the subduction shear zone. *Journal of petrology*, **55**(5), 883–916.

Burg, J. P., & Gerya, T. 2005. The role of viscous heating in Barrovian metamorphism of collisional orogens: thermomechanical models and application to the Lepontine Dome in the Central Alps. *Journal of Metamorphic Geology*, **23**(2), 75–95.

Carlson, R. L., & Miller, D. J. 2003. Mantle wedge water contents estimated from seismic velocities in partially serpentinized peridotites. *Geophysical Research Letters*, **30**(5).

Čížková, H., & Bina, C. R. 2013. Effects of mantle and subduction-interface rheologies on slab stagnation and trench rollback. *Earth and Planetary Science Letters*, **379**, 95–103.

Connolly, J. A.D. 2005. Computation of phase equilibria by linear programming: A tool for geodynamic modeling and its application to subduction zone decarbonation. *Earth and Planetary Science Letters*, **236**(1-2), 524–541.

Currie, C. A., Wang, K., Hyndman, R. D., & He, J. 2004. The thermal effects of steady-state slab-driven mantle flow above a subducting plate: The Cascadia subduction zone and backarc. *Earth and Planetary Science Letters*, **223**(1-2), 35–48.

Davies, J. H. 1999. The role of hydraulic fractures and intermediate depth earthquakes in generating suduction zone magmatism. *Nature*, **417**(March), 142–145.

England, P., & Katz, R. F. 2010. Melting above the anhydrous solidus controls the location of volcanic arcs. *Nature*, **467**(7316), 700–703.

England, P., Engdahl, R., & Thatcher, W. 2004. Systematic variation in the depths of slabs beneath arc volcanoes. *Geophysical Journal International*, **156**(2), 377–408.

Faccenda, M., Gerya, T., & Burlini, L. 2009. Deep slab hydration induced by bending-related variations in tectonic pressure. *Nature Geoscience*, **2**(11), 790–793.

Furukawa, Y. 1993. Magmatic Processes Under Arcs and Formation of the Volcanic Front. *Journal of Geophysical Research*, **98**, 8309–8319.

Gao, X., & Wang, K. 2014. Strength of stick-slip and creeping subduction megathrusts from heat flow observations. *Science*, **345**(6200), 1038–1041.

Gao, X., & Wang, K. 2017. Rheological separation of the megathrust seismogenic zone and episodic tremor and slip. *Nature*, **543**(7645), 416–419.

Gerya, T., & Yuen, D. A. 2003. Characteristics-based marker-in-cell method with conservative finite-differences schemes for modeling geological flows with strongly variable transport properties. *Physics of the Earth and Planetary Interiors*, **140**(4), 293–318.

Gonzalez, Christopher M, Gorczyk, Weronika, & Gerya, TV. 2016. Decarbonation of subducting slabs: Insight from petrological–thermomechanical modeling. *Gondwana Research*, **36**, 314–332.

Gorczyk, W., Willner, A. P., Gerya, T., Connolly, J. A.D., & Burg, J. P. 2007. Physical controls of magmatic productivity at Pacific-type convergent margins: Numerical modelling. *Physics of the Earth and Planetary Interiors*, **163**(1-4), 209–232.

Grove, T. L., Till, C. B., & Krawczynski, M. J. 2012. The Role of H 2 O in Subduction Zone Magmatism. *Annual Review of Earth and Planetary Sciences*, **40**(1), 413–439.

Hacker, B. R., Peacock, S. M., Abers, G. A., & Holloway, S. D. 2003. Subduction factory 2. Are intermediate-depth earthquakes in subducting slabs linked to metamorphic dehydration reactions? *Journal of Geophysical Research: Solid Earth*, **108**(b1).

Harlow, Francis H. 1962. *The particle-in-cell method for numerical solution of problems in fluid dynamics*. Tech. rept. Los Alamos Scientific Lab., N. Mex.

Harlow, Francis H. 1964. The particle-in-cell computing method for fluid dynamics. *Methods Comput. Phys.*, **3**, 319–343.

Hilairet, N., Reynard, B., Wang, Y., Daniel, I., Merkel, S., Nishiyama, N., & Petitgirard,

S. 2007. High-pressure creep of serpentine, interseismic deformation, and initiation of subduction. *Science*, **318**(5858), 1910–1913.

Hirauchi, Ken-ichi, Katayama, Ikuo, Uehara, Seiichiro, Miyahara, Masaaki, & Takai, Yasuhiro. 2010. Inhibition of subduction thrust earthquakes by low-temperature plastic flow in serpentine. *Earth and Planetary Science Letters*, **295**(3-4), 349–357.

Hyndman, R. D., & Peacock, S. M. 2003. Serpentinization of the forearc mantle. *Earth and Planetary Science Letters*, **212**(3-4), 417–432.

Ito, Keisuke, & Kennedy, George C. 1971. An experimental study of the basalt-garnet granulite-eclogite transition. *The structure and physical properties of the Earth's crust*, **14**, 303–314.

Karato, S., & Wu, P. 1993. Rheology of the upper mantle: A synthesis. *Science*, **260**(5109), 771–778.

McKenzie, D. P. 1969. Speculations on the Consequences and Causes of Plate Motions. *Geophysical Journal International*, **18**(1), 1–32.

Peacock, S. M. 1990. Fluid processes in subduction zones. *Science*, **248**(4953), 329–337.

Peacock, S. M. 1991. Numerical simulation of subduction zone pressure-temperature-time paths: constraints on fluid production and arc magmatism. *Philosophical Transactions of* *the Royal Society of London. Series A: Physical and Engineering Sciences*, **335**(1638), 341–353.

Peacock, S. M. 1993. The importance of blueschist $\rightarrow$ eclogite dehydration reactions in subducting oceanic crust. *Geological Society of America Bulletin*, **105**(5), 684–694.

Peacock, S. M. 1996. Thermal and petrologic structure of subduction zones. *Subduction: top to bottom*, **96**, 119–133.

Peacock, S. M., & Hyndman, R. D. 1999. Hydrous minerals in the mantle wedge and the maximum depth of subduction thrust earthquakes. *Geophysical Research Letters*, **26**(No. 16), 2517–2520.

Peacock, S. M., Rushmer, T., & Thompson, A. B. 1994. Partial melting of subducting oceanic crust. *Earth and planetary science letters*, **121**(1-2), 227–244.

Plümper, Oliver, John, Timm, Podladchikov, Yuri Y, Vrijmoed, Johannes C, & Scambelluri, Marco. 2017. Fluid escape from subduction zones controlled by channel-forming reactive porosity. *Nature Geoscience*, **10**(2), 150–156.

Ranalli, G. 1995. *Rheology of the Earth*. Springer Science & Business Media.

Reynard, B. 2013. Serpentine in active subduction zones. *Lithos*, **178**, 171–185.

Ruh, J. B., Le Pourhiet, L., Agard, P., Burov, E., & Gerya, T. 2015. Tectonic slicing of subducting oceanic crust along plate interfaces: Numerical modeling. *Geochemistry, Geophysics, Geosystems*, **16**(10), 3505–3531.

Schmidt, M. W., & Poli, S. 1998. Experimentally based water budgets for dehydrating slabs and consequences for arc magma generation. *Earth and Planetary Science Letters*, **163**(1-4), 361–379.

Shen, T., Hermann, J., Zhang, L., Lü, Z., Padrón-Navarta, J. A., Xia, B., & Bader, T. 2015. UHP metamorphism documented in Ti-chondrodite-and Ti-clinohumite-bearing serpentinized ultramafic rocks from Chinese southwestern Tianshan. *Journal of Petrology*, **56**(7), 1425–1458.

Sizova, E., Gerya, T., Brown, M., & Perchuk, L. L. 2010. Subduction styles in the Precambrian: Insight from numerical experiments. *Lithos*, **116**(3-4), 209–229.

Syracuse, E. M., & Abers, G. A. 2006. Global compilation of variations in slab depth beneath arc volcanoes and implications. *Geochemistry, Geophysics, Geosystems*, **7**(5).

Syracuse, E. M., van Keken, P. E., Abers, G. A., Suetsugu, D., Bina, C. R., Inoue, T., Wiens, D., & Jellinek, M. 2010. The global range of subduction zone thermal models. *Physics of the Earth and Planetary Interiors*, **183**(1-2), 73–90.

van Keken, P. E., Hacker, B. R., Syracuse, E. M., & Abers, G. A. 2011. Subduction factory: 4. Depth-dependent flux of H 2 O from subducting slabs worldwide. *Journal of Geophysical Research*, **116**(b1), b01401.

van Keken, P. E., Wada, I., Abers, G. A., Hacker, B. R., & Wang, K. 2018. Mafic High-Pressure Rocks Are Preferentially Exhumed From Warm Subduction Settings. *Geochemistry, Geophysics, Geosystems*, **19**(9), 2934–2961.

Wada, I., & Wang, K. 2009. Common depth of slab-mantle decoupling: Reconciling diversity and uniformity of subduction zones. *Geochemistry, Geophysics, Geosystems*, **10**(10), n/a–n/a.

Wada, I., Wang, K., He, J., & Hyndman, R. D. 2008. Weakening of the subduction interface and its effects on surface heat flow, slab dehydration, and mantle wedge serpentinization. *Journal of Geophysical Research: Solid Earth*, **113**(4), 1–15.

Wada, I., Behn, M. D., & Shaw, A. M. 2012. Effects of heterogeneous hydration in the incoming plate, slab rehydration, and mantle wedge hydration on slab-derived H 2O flux in subduction zones. *Earth and Planetary Science Letters*, **353-354**, 60–71.

Wilson, C. R., Spiegelman, M., van Keken, P. E., & Hacker, B. R. 2014. Fluid flow in subduction zones: The role of solid rheology and compaction pressure. *Earth and Planetary Science Letters*, **401**, 261–274.

Zack, Thomas, & John, Timm. 2007. An evaluation of reactive fluid flow and trace element mobility in subducting slabs. *Chemical Geology*, **239**(3-4), 199–216.